RESEARCH ARTICLE

A comprehensive investigation of trailing edge damage in a wind turbine rotor blade

Philipp Ulrich Haselbach, Martin Alexander Eder and Federico Belloni

Department of Wind Energy, Technical University of Denmark, Kgs. Lyngby, Frederiksborgvej 399, 4000 Roskilde, Denmark

ABSTRACT

Wind turbine rotor blades are sophisticated, multipart, lightweight structures whose aeroelasticity-driven geometrical complexity and high strength-to-mass utilization lend themselves to the application of glass-fibre or carbon-fibre composite materials. Most manufacturing techniques involve separate production of the multi-material subcomponents of which a blade is comprised and which are commonly joined through adhesives. Adhesive joints are known to represent a weak link in the structural integrity of blades, where particularly, the trailing-edge joint is notorious for its susceptibility to damage. Empiricism tells that adhesive joints in blades often do not fulfil their expected lifetime, leading to considerable expenses because of repair or blade replacement. Owing to the complicated structural behaviour—in conjunction with the complex loading situation—literature about the root causes for adhesive joint failure in blades is scarce. This paper presents a comprehensive numerical investigation of energy release rates at the tip of a transversely oriented crack in the trailing edge of a 34m long blade for a 1.5MW wind turbine. First, results of a non-linear finite element analysis of a 3D blade model, compared with experimental data of a blade test conducted at Danmarks Tekniske Universitet (DTU) Wind Energy (Department of Wind Energy, Technical University of Denmark), showed to be in good agreement. Subsequently, the effects of geometrical non-linear cross-section deformation and trailing-edge wave formation on the energy release rates were investigated based on realistic aeroelastic load simulations. The paper concludes with a discussion about critical loading directions that trigger two different non-linear deformation mechanisms and their potential impact on adhesive trailing-edge joint failure. Copyright © 2016 John Wiley & Sons, Ltd.

1. INTRODUCTION

Wind turbine rotor blades are sophisticated multipart, multi-material, lightweight structures. The aeroelastic optimisation of the lift-generating surfaces that maximize power production leads to complex curved asymmetric geometries, which involve taper, twist and curvature. The use of glass-fibre or carbon-fibre composite materials for blades lends itself because of shape manufacturability and their desirable high strength to low mass ratios. Most manufacturing techniques involve the separate production of the many subcomponents of which a blade is comprised and which are fittingly connected via adhesive joints.

Empirical evidence presented by Ataya and Ahmed[1] shows that, exactly those adhesive joints present a weak link in the structural integrity of blades, where particularly, the trailing-edge joint is notorious for its susceptibility to damage. Adhesive joints that do not fulfil their expected lifetime result in considerable cost expenses because of downtime, repair and—even worse—blade replacement.

According to a study from the *National Renewable Energy Laboratory* published in a report by Sheng,[2] the contribution of rotor issues to the total downtime of a wind turbine ranges between 8% and 20%.

Just recently, it was announced in an article by Wittrup[3] that all rotor blades in the Horns Rev2 wind park in Denmark are about to be replaced. The observed damage types of the rotor blades covered a wide range of failure types. Many

of the observed damages concerned leading and trailing-edge issues. Consequently, research on structural problems that may improve blade designs, and hence, increase lifetime offers a great cost saving potential for blade manufacturers as well as operators. However, literature dedicated to adhesive joint failure in wind turbine rotor blades is scarce. One of the underlying reasons is that the interplay of the various structural effects lead to inherently complex structural behaviour.

In blades, the cross-section warping deformations are associated with different modal *strain energy release rates* (SERRs). Such deformations are caused by both linear and non-linear effects. It appears that in blades, linear effects on SERRs are largely due to out-of-plane warping. The latter is mainly caused by shear and torsion, both of which induce mode-III SERRs as discussed in.[4] Geometrical effects such as taper, add to the problem by altering the shear flow distribution and therefore affect the mode-III SERRs. In addition, the use of materials with different Poisson's ratio between subcomponents can induce linear effects owing to the additional fracture modes struggle to deform at different rates.

Regarding the non-linear effects, note that wind turbine blades are beam-type structures with thin-walled cross-sections made from orthotropic materials. Using composite materials allows blades to undergo tip deformations of up to 20% of their span. These large deflections, in conjunction with high out-of-plane and low in-plane cross-section stiffness, lead to geometric non-linear in-plane cross-section deformations. This bending-induced in-plane warping effect—also referred to as *Brazier effect* or *cross-section ovalisation* as investigated for blades by Damkilde and Lund[5] as well as Cecchini and Weaver[6]—is typically associated with mode-I and mode-II SERRs as discussed in.[7–9] The formation of geometrically non-linear lengthwise wave deformation patterns in the trailing edge increases the severity. In this case, the SERR magnitudes increase exponentially, leading to unstable crack growth as discussed in[10]

Rotor blade trailing edges are very sensitive to stability effects like e.g. local buckling or fibre kinking, which are usually caused by geometrical imperfections. Small manufacturing deviations with respect to the trailing-edge shape or the fibre alignment can affect the structure significantly. Also, the load carrying capacity of wind turbine rotor blades is highly depending on the load direction and magnitude. While rotor blades can deal with high flapwise bending moments, load direction exposing the trailing edge to compressive stresses with lower magnitudes can lead to trailing-edge buckling and failure.

Figure 1 shows an overview of a cause-and-effect analysis of trailing-edge failure based on a system engineering framework to the structural integrity concept presented by Hoeppner.[11] The *holistic structural integrity process* is based on the fundamental idea that failure modes or mechanisms are interconnected and considers all fracture mechanisms for monotonic loading with consideration of the intrinsic nature of solids.[11] Beside the here-presented interaction of different failure modes, external conditions like e.g. temperature, chemical environments, humidity and radiation are not listed, but affecting the trailing-edge reliability, too.

This paper aims at a comprehensive approach by simultaneously considering the aforementioned linear and non-linear effects and their interplay implicitly in the model and the test structure. The conducted work could serve as a basis for a holistic structural integrity process of trailing-edge failure. This investigation sheds light on both the SERRs and mode mixity of a crack in the trailing-edge joint of a 34m long blade for a 1.5MW wind turbine. The introduced crack represents
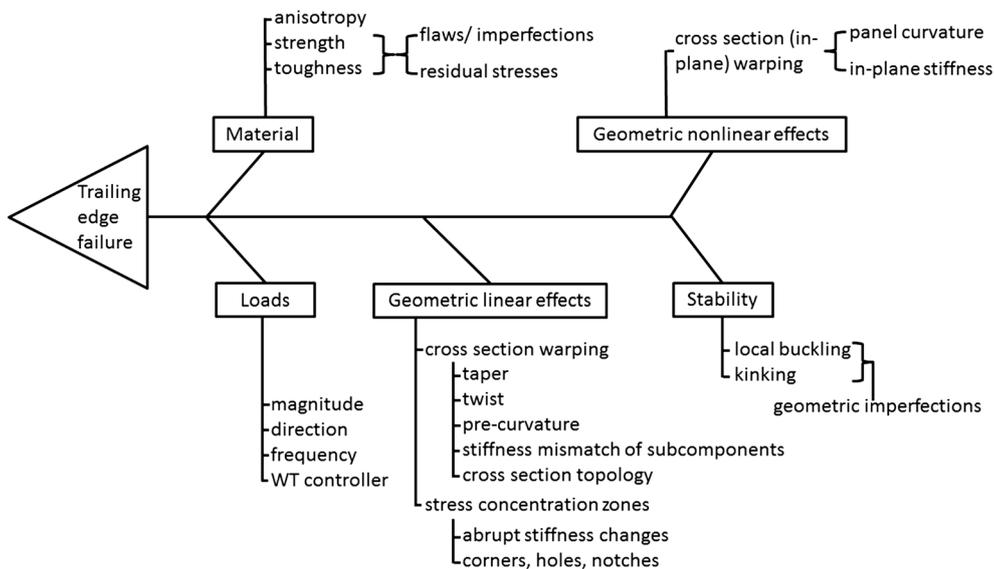

Figure 1. Cause and effect analysis of trailing-edge failure.

a flaw that runs along the internal fillet edge of the adhesive. It is beyond the scope of this paper to perform crack growth analysis. Instead, the crack in the adhesive served as an indicator and was used to study the prevailing fracture modes as functions of the load magnitude and its direction.

Initial experimental results of a four-point loading blade test conducted at DTU Wind Energy are presented. The measurement methodology aimed at the detection of a wave as it formed in the trailing edge and which eventually led to brittle debonding of the trailing-edge joint. Subsequently, aeroelastic simulation results are used to create a realistic load envelope, which serves to benchmark the loads applied during the experiment. A detailed numerical 3D model of the blade is first validated against the test data and subsequently used to investigate SERRs in the trailing edge for the aeroelastic load envelope. The paper concludes with a discussion of critical loading directions and their associated SERRs, as caused by cross-section deformation and geometrically non-linear wave formation.

2. METHODS

2.1. Experimental setup

The tested wind turbine rotor blade with an original length of 34m was truncated at 29.5 m to accommodate it in the blade-testing facility at DTU Wind Energy. The root of the blade was bolted to a reaction frame at a pitch angle of 120° as shown in Figure 2(a), which refers to a bending moment angle of 210° (Section 2.5). Figure 2(b) shows that the blade was loaded at four loading points (LPs) by means of carbon steel anchor plates (approximately 0.4m × 0.4m × 0.015m). Steel wires were attached to the carbon steel anchor plates, which were adhesively connected underneath the suction side cap. Additional blind bolts were used to reinforce the connection. The loads were applied by pulleys in connection with displacement-controlled winches that pulled the blade towards the floor. The forces in the LPs could be measured by interconnected load cells as shown in Figure 2(a).

The loading procedure of the blade is a non-linear problem. During the loading process, individual LPs unload because of structural coupling effects, thereby rendering a multiple-point loading scheme uncertain with regard to meeting repeatability and accuracy demands. The loads were therefore applied at a quasistatic rate of ≤ 0.1 m min^{-1} in an iterative procedure until a convergence threshold was reached for every LP. The convergence threshold was defined as 2% rela-
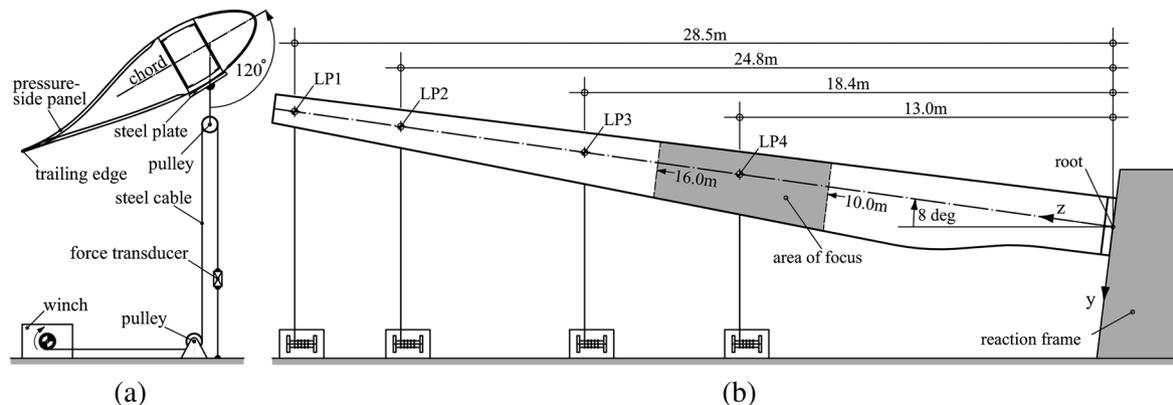

Figure 2. (a) Cross section with pulley system and force transducer and b) elevation of test setup with loading point (LP) positions and area of measurement focus.

Table I. Normalized target loads at LPs for specific key load steps as will be referred to in subsequent sections.

Load step	LP1	LP2	LP3	LP4
57%	0.57	0.53	0.44	0.44
67%	0.67	0.63	0.52	0.52
76%	0.76	0.71	0.59	0.59
90% (MDL)	0.90	0.84	0.70	0.70
100% (ultimate)	1.00	0.94	0.78	0.78

LPs, loading points; MDL, maximum design load.

tive error between the measured force and the target load. During this iterative procedure, every LP starting with LP1 was brought up to the target load individually and irrespective of the response of the inactive LPs. This procedure was repeated in so-called loops until the convergence threshold was satisfied in all individual LPs at every load step. Typically, 15 to 20 loops per load step were needed to satisfy the convergence threshold in all four LPs. Table I gives the individual loads normalized with LP1 (tip) for different key load steps where the load ratios between the LPs are constant.

2.2. Conventional sensors

Quasi-vertical displacements of the blade were measured with *ASM Posiwire 6250* (ASM) draw wire transducers and will be referred to as ASMs in this paper. Four ASMs were mounted on the strong floor with the draw wires attached to the suction-side cap at 10.0, 16.0, 22.0 and 29.0 m. Two additional ASMs were directly attached to the trailing edge at 13.0 and 16.0 m to validate the optical displacement measurements described in Subsection 2.4. Electrical resistance strain gauges were used to validate longitudinal strains in the vicinity of the fibre sensors discussed later in Subsection 3.2. These complementary strain gauges were glued directly on to the laminate after gelcoat removal and surface preparation.

2.3. Fibre sensors

Commercial fibre-sensing equipment from *HBM FiberSensing* was used to measure both longitudinal and transverse surface strains along the adhesive trailing-edge joint. The sensors were directly glued on the laminate after the gelcoat was ground off and the surface degreased and cleaned. The convention for the measurement direction *longitudinal* and *transverse* is stipulated in Figure 3(a). The measurement principle is based on Bragg reflection as explained in Hill,[12] Kersey,[13] Morey[14] and Kashyap.[15] *Fibre Bragg grating* (FBG) sensors are introduced into an optical fibre along a gauge length of approximately 4 mm at customized spacings. Each FBG sensor represents a crystallographic plane, which reflects a specific wave length of the light spectrum travelling through the fibre and appears as a specific power output peak. Any elongation or contraction of the sensor causes a phase shift of the reflected wave, which is proportional to the change of strain in the sensor. The strain measurable bandwidth is an inverse function of the amount of sensors in a fibre line. In the adopted configuration, a band width (of 2.9 nm which is) equal to $\pm$ 2400 μm /m was considered a proper compromise in order to have 10 sensors per fibre line. Examples of fibre applications for wind turbine rotor blades appear in Schroeder[16] and Fattahi.[17]

The sensor setup was designed to measure the wave formation in the trailing edge even at low load levels through the variation of longitudinal bending strains along the wave. For this purpose, a coarse sensor array with sensors spaced every 0.4 m was used to measure longitudinal strains on the pressure side between 10.0 and 23.6 m. A refined sensor array with sensors spaced every 0.15 m was applied on the pressure side in the designated failure area between 10.0 and 16.0 m. Transverse strains were measured on the pressure-side and the suction-side shell at 0.15 m intervals adjacent to the longitudinal sensors in the designated failure area. The sensor scheme of all measurement lines with a total of 160 sensors is shown in Figure 3(a), whereas the location of the sensors relative to one another in respect to the trailing edge appears in Figure 3(b).
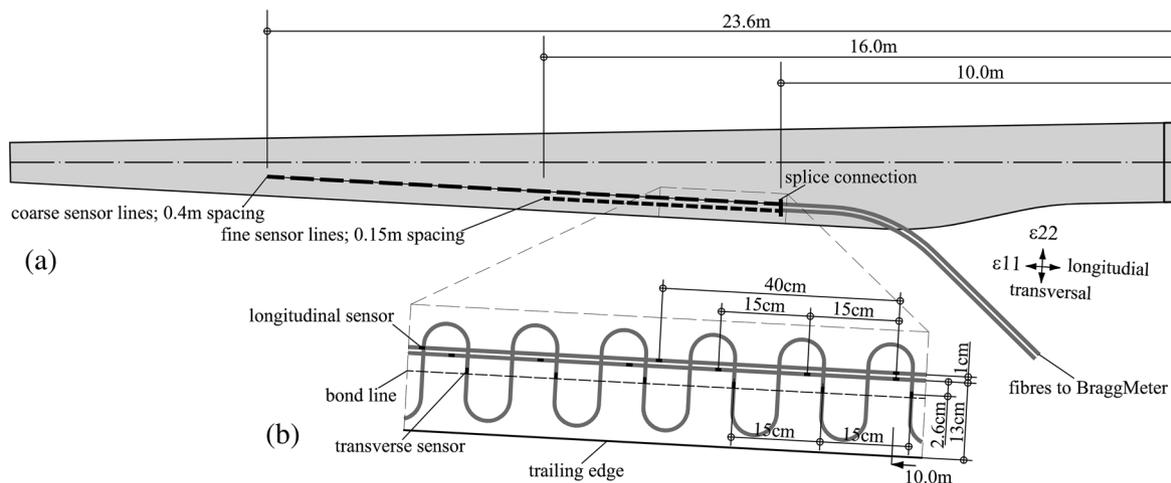

Figure 3. Position of fibre sensors.

All sensors were connected to two spectrometers (*BraggMeters*) with a laser-wave length range between λ =1500 and λ =1600 nm. Each fibre contained 10 sensors with a measurement wave-length range of $\Delta\lambda = \pm 5$ nm, which gave a strain measurement bandwidth of $\Delta\epsilon = 1000\Delta\lambda/1.2$ =4167 μm m^{-}1 where the factor 1.2 is a photo-optical constant.

2.4. Optical displacement measurement

An in-house stereo photogrammetry measurement system was used to measure the 3D displacements of marker points on the trailing edge, as shown in Figure 4(c) and (d). The markers were placed at 0.25 m intervals between 12.5 and 16.0 m with the purpose of tracking the trailing-edge wave deformation. The pattern of the black and white marker points (Figure 4(c)) enabled the recognition of the marker point centres by means of the *automated image processing software*. The measurement methodology is based on the pinhole camera principle as described by Atkinson.[18] A description of the *automated image processing software* appears in.[7] The stereo photogrammetry principle requires a pair of simultaneously taken images containing both a calibration grid and the measurement object. In the first step of its application, the real-world coordinates and its corresponding image coordinates of the calibration grid are used for camera calibration. In a subsequent step, the camera calibration parameters are used together with the image coordinates of the measurement object to triangulate its real world.

For this purpose, two Samsung ST200 cameras (Samsung Group, Seoul, Korea) were mounted at a rigid elevated position parallel to the trailing edge. Both cameras covered the same measurement area including the calibration grid shown in Figure 4(a) and (b). Shown in Figure 4(d), the calibration grid consisted of two staggered parallel planes with an offset of 5.0e-2 m. Both planes featured a black and white checker-board pattern with a square size of 5.0e-2 m. The calibration grid was placed underneath the trailing edge and aligned with a laser level. A pair of images corresponding to one measurement was simultaneously taken prior to loading, and then at every load step. In order to determine the accuracy of the camera system, the error between the known real world coordinates of the calibration grid and those obtained by triangulation was computed. The error followed normal distribution, where the standard deviations in the x, y and z-directions were δ_x=2e-4, δ_y=3e-4 and δ_z=7e-4 m, respectively.

2.5. Aeroelastic simulations

DTU's aeroelastic software package *horizontal axis wind turbine Code* HAWC2 11.9[19, 20] was used to perform aeroelastic simulations in order to predict bending moment distributions along the blade, and to determine forces at the cross sections
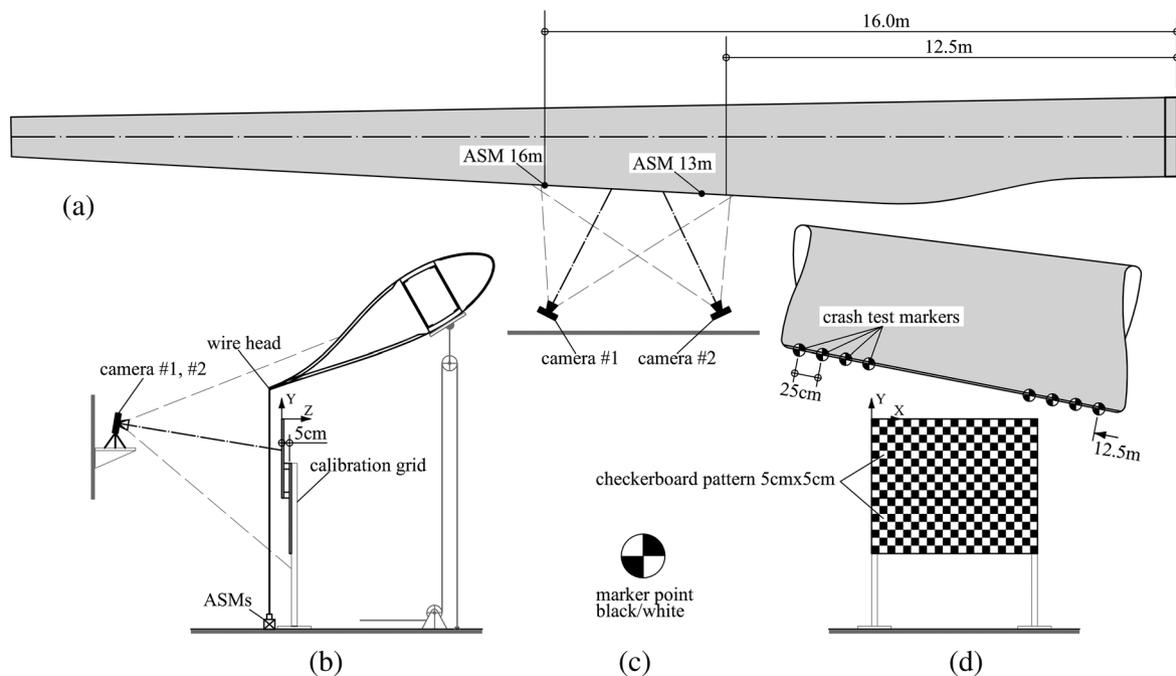

Figure 4. (a) Plane view of the blade with two cameras, (b) cross section of the blade with elevation showing position of cameras and calibration grid, (c) marker point and (d) calibration grid and position of marker points from the camera's perspective and measurement coordinate system.

of the blade for various loads. The aeroelastic bending moments were used to benchmark the applied loads during the blade test. Furthermore, the simulations enabled the computation of SERRs based on load distributions that the blade would experience during operation.

The airfoil characteristics and cross-section rigidity of the tested 34 m long blade were modelled according to manufacturer specifications for the aeroelastic simulations. However, hub, tower and generator properties were not based on the originally designed platform, but instead based on the Neg Micon NM80 turbine platform[21] with a stated rated power of 2.3 MW.

Although the blade being studied is designed for wind turbines with a rated power of 1.5 MW, the turbine used was considered acceptable because of a similar blade length of 38.8 m. The wind turbine was consequently downrated to 1.5 MW, and the proportional and integral feedback controller (PI-controller) was optimized for the new setup using DTU's aeroservoelastic stability tool *HAWCStab2* (Roskilde, Denmark).[22]

The *design load cases* (DLCs) as directed by IEC-61400-1[23] were simulated for different levels of turbulence (seeds) and yaw misalignment. The aeroelastic simulations provided the time history of the bending moment vector components $M_x(t)$ and $M_y(t)$ in 17 cross-sections along the blade. A 3D bending moment envelope was generated by plotting the maximum bending moment values, which occurred during the simulation time in a specific DLC in the cross sections along the blade. Two different bending moment envelopes were generated: The first one—denoted as *CBM*—refers to a *constant bending moment*, corresponding in its magnitude to approximately 57% of the ultimate load of the blade test. The second—denoted as *MDL*—refers to the *maximum design load* in this paper. The *MDL* comprises all DLCs defined in.[23] The bending moments extracted from aeroelastic simulations were multiplied by the corresponding DLC safety factor. An exception was DLC1.1, where the simulations were multiplied by a safety factor of 1.25 according to[23] but the 50-year extrapolation usually required was omitted because the wind turbine site was unknown.

The bending moment magnitudes M_i obtained from the envelope equation (1) can be used to calculate the force magnitudes F_i, which create a bending moment distribution that emulates those obtained from aeroelastic simulations. These forces were consequently used to load the numerical blade model as discussed in Subsection 2.6.

$$\begin{pmatrix} F_1 \\ F_2 \\ F_3 \\ F_4 \end{pmatrix} = \begin{bmatrix} \frac{1}{z_1-z_2} & 0 & 0 & 0 \\ \frac{z_3-z_1}{(z_2-z_3)(z_1-z_2)} & \frac{1}{z_2-z_3} & 0 & 0 \\ \frac{1}{z_2-z_3} & \frac{z_4-z_2}{(z_3-z_4)(z_2-z_3)} & \frac{1}{z_3-z_4} & 0 \\ 0 & \frac{1}{z_3-z_4} & \frac{-z_3}{(z_3-z_4)z_4} & \frac{1}{z_4} \end{bmatrix} \cdot \begin{pmatrix} M_2 \\ M_3 \\ M_4 \\ M_5 \end{pmatrix} \tag{1}$$

Indices 1–4 represent the locations of the force application points; index 5 represents the root, M_i represents the aeroelastic bending moment magnitude, F_i represents the force magnitudes and z_i denotes the lengthwise position of the individual force application points (Figure 5(a)).

Figure 5(b) shows the polar coordinate system defining the bending moment vector and its angular direction α. The associated force vector obtained from equation (1) was transformed into the components F_x and F_y of the cross-section coordinate system. A so-called load envelope was generated for *MDL* by plotting the load components at the force application points.
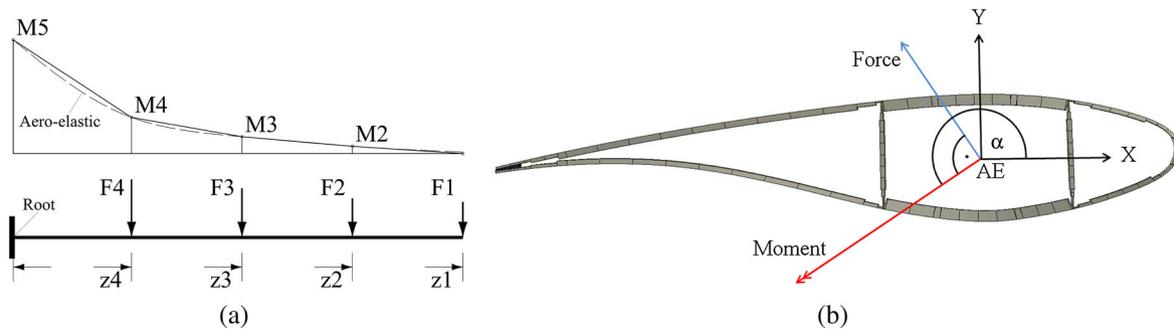

Figure 5. (a) Schematic bending moment distribution along the blade and (b) cross section coordinate system and loading directions with bending moment vector and force vector. The angle α represents the direction of the bending moment vector measured counter-clockwise from the X-axis.

Table II. Properties of the composite material in the trailing edge where the abbreviations pre-preg (pre-impregnated composite fibers) (*Pre*), High Resin Content (*HRC*) and UniDirectional laminate (*UD*) denote pre-preg, high resin content and unidirectional laminate, respectively.

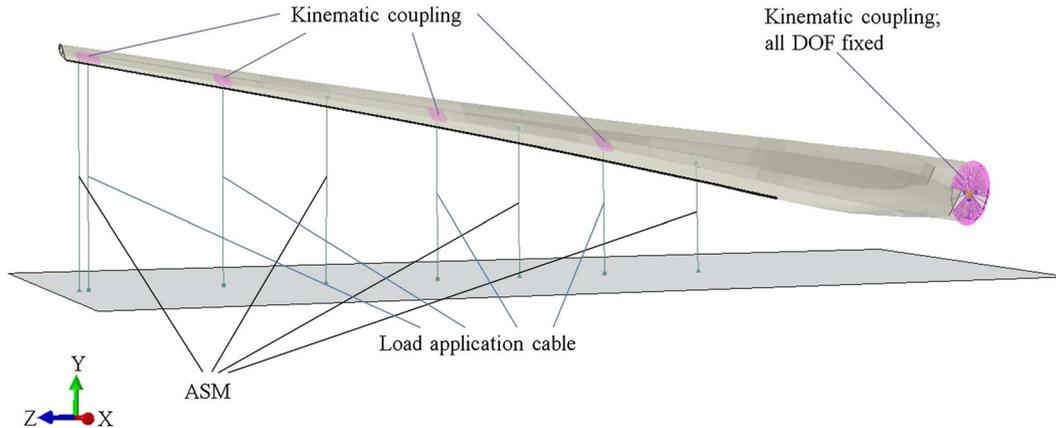| Properties	Biaxial Pre	Biaxial	Triaxial	Triaxial HRC	UD	Adhesive	Unit
ρ	1890	1894	1864	1683	1931	1180	kg/m^{-3}
E_{11}	11.58	12.75	20.26	16.70	41.26	3.00	GPa
E_{22}	11.58	12.75	10.42	8.59	11.39	3.00	GPa
ν_{12}	0.50	0.50	0.50	0.50	0.33	0.38	—
$G_{12} = G_{13}$	10.66	10.06	7.35	6.61	3.91	1.09	GPa
G_{23}	4.00	4.00	4.00	4.00	3.91	1.09	GPa

Figure 6. Wind turbine blade model simulating test conditions for validation. Boundary conditions at the root and both loading points and ASMs modelled with axial connector elements tied to the strong floor. DOF, degrees of freedom.

2.6. Finite element analysis

The structural blade design is composed of a box girder connected to the pressure-side and suction-side panel that form the aerodynamic surface. Panels are themselves connected by a trailing-edge joint and a leading-edge joint. The software package *Abaqus* 6.13[24] was used for structural analyses of the blade. The panels and box-girder were discretized with 6.7e4 8-node doubly curved thick shell elements with reduced integration (Abaqus type S8R). The characteristic element length was 5.0e-2 m. The shell elements were placed at the outer surface of the blade model and had an offset corresponding to half the material thickness. The adhesive of the trailing-edge joint was discretized with four layers of 2.75e5 8-node linear brick elements with reduced integration and hourglass control (Abaqus type C3D8I). The adhesive with a constant bond length of 8.0e-2 m and a characteristic element size of 5.0e-3 m was felt to provide sufficient accuracy for the *virtual crack closure technique* (VCCT). Tie constraints were used to connect the brick elements to the shell elements.

The elastic material properties of the trailing-edge laminate layup components—as well as the properties of the isotropic epoxy-based adhesive—are listed in Table II. Indices 1 and 2 refer to the 0° and 90° material directions, respectively, E_{ij} represents the elastic modulus, G_{ij} represents the shear modulus and ν_{ij} denotes Poisson's ratio.

A kinematic (rigid) coupling constraint was applied to the nodes of the root section. All six degrees of freedom of the master node located in the elastic centre of the root section were restrained. The four anchor plates were assumed to be rigid and hence, modelled through kinematic coupling constraints tied to the master nodes of each LPs (Figures 6 and 7). For model validation, the load was applied by axial contraction of connector elements. This follower force approach is a realistic representation of the experimental loading conditions. Axial connector elements were also used to model the draw wire transducer (ASM) measurement principle, thereby enabling a direct comparison between measurements and numerical results.

All numerical simulations were performed as quasistatic simulations including geometric non-linearity. For most of the simulations, the Abaqus standard Newton–Raphson solver technique was used. In load cases associated with geometrically non-linear wave formation, equilibrium could not be reached with the standard solver for higher loads. In order to overcome these convergence problems, an implicit dynamic solver was chosen instead. The loads were linearly ramped up over a period of 10 s so the kinetic energy was at least two orders of magnitude smaller than the strain energy in each time increment. A viscosity coefficient of 1e-4 was used to stabilize the numerical simulations.
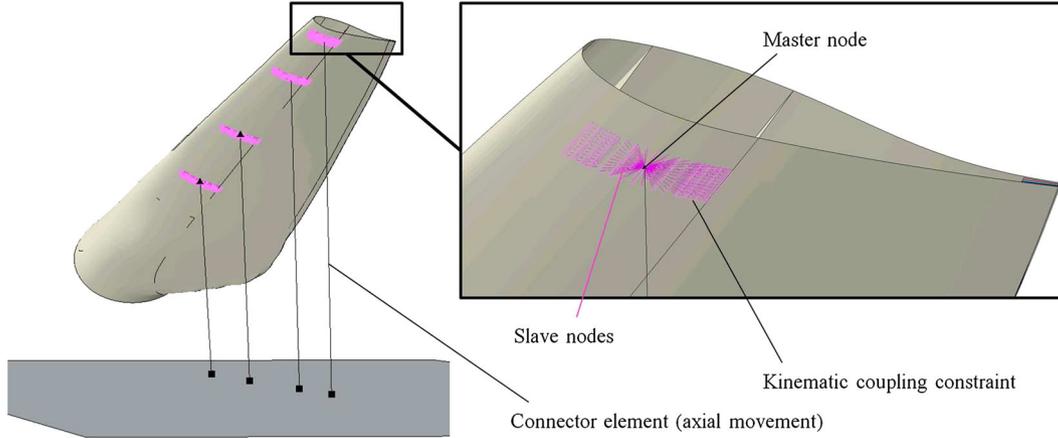
Figure 7. Detail of kinematic coupling constraint used to model the load, similar to the blade test.
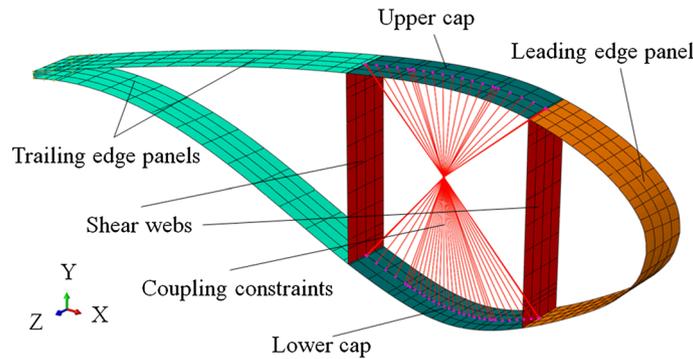

Figure 8. Blade model cross-section slice with main parts and continuum distributing coupling constraints connected to the shell nodes of the caps with a central master node at the aeroelastic centre.

For fracture analysis, the force application scheme described earlier was modified in order to ease the multidirectional loading procedure. Continuum distributing coupling constraints[24] were assigned to the cross sections at 13.12, 18.6, 25.04 and 28.78 m in order to avoid restraining cross-section warping. Loads were applied as concentrated forces at the individual master nodes located in the aeroelastic centres of the cross sections. Figure 8 shows the distributed coupling constraints at 13.12 m.

The VCCT tool in Abaqus was used to compute the SERRs in a 1.0e-2 m crack introduced in the mid-surface of the adhesive trailing-edge joint (Figure 9).

Hard normal contact conditions and tangential frictionless contact conditions were assigned to the crack surfaces to prevent material interpenetration. For a detailed description of the VCCT, the reader is referred to Krueger[25] and.[24] Equations (2) and (3) were used to compute the in-plane (ψ) and out-of-plane (ϕ) mode mixity angles.

$$\psi = arctan\sqrt{\frac{G_{II}}{G_I}} \tag{2}$$

$$\phi = arccos\sqrt{\frac{G_{III}}{G_I + G_{II} + G_{III}}} \tag{3}$$

where G_I, G_{II} and G_{III} are the modal SERRs obtained by the VCCT.

Kenane and Benzeggagh[26] suggest that a crack propagates when G_{tot} given in equation (4) exceeds G_{equ} given by equation (5). Equation (5) was used to determine the proximity to crack initiation and to obtain the critical loading directions.

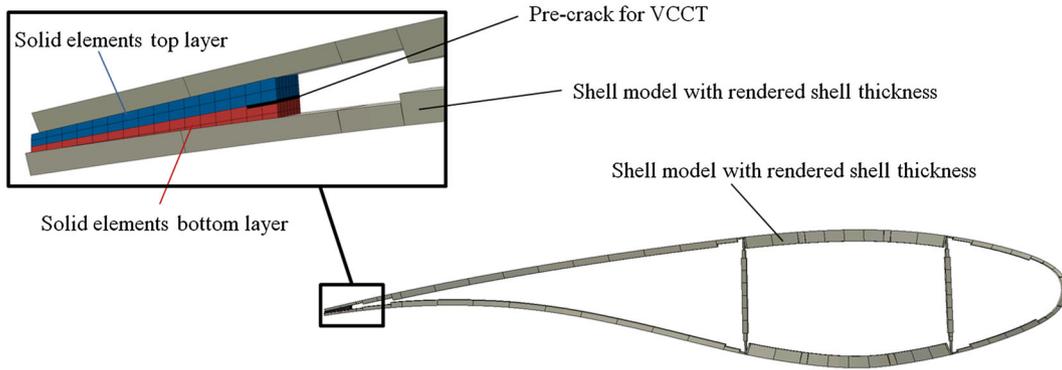$$G_{tot} = G_I + G_{II} + G_{III} \tag{4}$$

Figure 9. Cross-section slice with rendered shell elements and detail of solid element discretization of the adhesive in the trailing edge. A crack of 1.0e-2 m is located between the top and bottom solid element layer of the adhesive bondline. Tie constraints connect the solid elements to the shell elements. VCCT, virtual crack closure technique.

$$G_{equ} = G_{Ic} + (G_{IIc} - G_{Ic}) \left(\frac{G_{II} + G_{III}}{G_I + G_{II} + G_{III}} \right)^{\eta} \tag{5}$$

where G_{Ic} and G_{IIc} are the experimentally obtained critical mode-I and mode-II SERRs. For the sake of simplicity, the initiation fracture energies G_{Ic}=665 J m^{-2} and G_{IIc}=1216 J m^{-2} of fillet detail *Type B* in [10, Figure 5(b) and Table 1] were used. The exponent was set to $\eta = 2$ for brittle resins.

2.7. Wave extraction techniques

In an attempt to separate the local trailing-edge wave from the total global displacements, two different approaches were used.

The first approach is based purely on experimental results where the total global displacements are described by equation (6). It was found that a third-order polynomial fits the measured cap deformations given in Table III and was consequently used for the base deformation of the trailing edge. The local wave portion was approximated by a sine function within the measurement interval.

$$u_y(z) = a_0 z + a_1 z^2 + a_2 z^3 + a_3 \sin(fz) \tag{6}$$

where z represents the lengthwise position measured from the root, and both $a_{0,1,2,3}$ and f are constants. The constants of equation (6) were iteratively obtained by a non-linear least square method using the MATLAB curve fitting tool.[27]

The second approach is a hybrid method combining numerical results and measurement values, which allows more data points to be considered than in the first approach. It was found that the polynomial given by equation (7) fits the numerically obtained global trailing-edge deformation between 7.0 and 29.5 m at a low load level where the wave was imperceptible. Equation (7) was therefore assumed to represent the base deformation of the trailing edge in absence of the wave. The fitting constants were obtained in MATLAB[27] by a non-linear least square method. The local wave was obtained by subtracting the base deformation from the measured or numerically predicted total global displacements.

$$u_y(z) = a_0 z^5 + a_1 z^4 + a_2 z^3 + a_3 z^2 + a_4 z + a_5 \tag{7}$$

where z represents the lengthwise position measured from the root and $a_{0,1,2,3,4,5}$ are curve-fitting constants.

3. RESULTS

3.1. Aeroelastic simulation results

Figure 10(a) shows a normalized contour plot of the root bending moment envelope for MDL. The dashed lines indicate the angular direction of the experimentally applied bending moment at $\alpha = 210°$ and the two critical angular directions ($\alpha = 135°$ and $\alpha = 240°$) as discussed in Section 3.3. The highest bending moment magnitude occurred for $\alpha = 163°$.

Figure 10(b) shows the spanwise bending moment distribution of MDL at an angular direction of $\alpha = 210°$ and the maximum applied load during the experiments. The latter is denoted as *ultimate load* (UL) and defined as 100%, whereas the MDL corresponds to approximately 90% of the applied ultimate load. Figure 10(b) shows that the experimentally
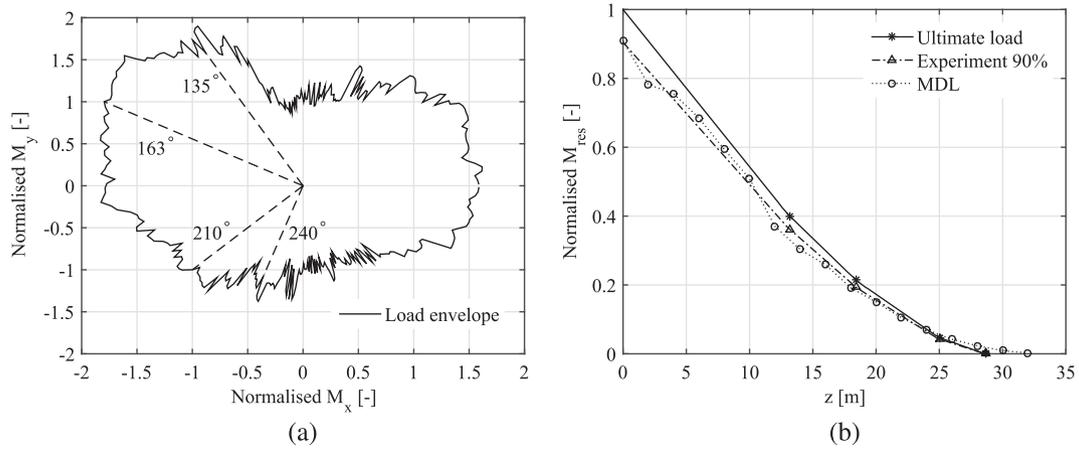
(a)   (b)

Figure 10. (a) Bending moment contour plot for maximum design load (MDL) and angular directions for selected load cases and (b) comparison of maximum applied bending moment during the experiments and extracted bending moment (MDL) from aeroelastic load calculations.

Table III. Experimentally and numerically obtained global cap deformations at four different measurement points for the 76% load step.

	z = 29.5 m	z = 22.0 m	z = 16.0 m	z = 10.0 m	Unit
ASM	−1.914	−0.7974	−0.307	−0.102	m
Numeric	−1.880	−0.8023	−0.311	−0.102	m
Rel. error	−1.77	0.62	1.38	0.00	%

Table IV. Experimentally and numerically obtained global trailing-edge deformations for three load steps.

Load step	ASM 13 m	Optic 13 m	Numeric 13 m	ASM 16 m	Optic 16 m	Numeric 16 m
%	m	m	m	m	m	m
57	−0.113	−0.114	−0.113	−0.204	−0.204	−0.206
67	−0.130	−0.132	−0.129	−0.237	−0.236	−0.238
76	−0.149	−0.150	−0.143	−0.271	−0.274	−0.270

applied bending moment distributions closely resemble those obtained from aeroelastic simulations. The MDL functioned as a reference load in order to evaluate the UL under which the blade failed.

3.2. Experimental results and model validation

The numerical blade model was first validated against experimental data for the load case presented in Subsection 2.1. Table III lists the measured and numerically obtained cap deformations. The maximum relative error was less than 2% at the blade tip.

Figure 11(a) shows the trailing-edge deformation from the perspective of camera 2 at a load step of 57% at the onset of the wave. Figure 11(b) shows the trailing edge at a load step of 76% with a distinct wave in the centre of the measurement length.

Table IV lists the vertical trailing-edge displacements at 13 and 16 m obtained by ASM measurements and numerical analysis for three subsequent load steps of 57%, 67% and 76%.

The graphs in Figure 12(a) and (b) represent the first wave extraction approach described in Section 2.7.

Figure 12(a) shows that the solid graph given by equation (6) fits the optical measurement data (circular markers) well. Figure 12(b) shows that in the wave given by the last term of equation (6), the peak shifted slightly towards the tip with increasing load. The amplitude progressively increased from 2e-3 to 6e-3 m. The wave length $\Lambda = 2\pi/f$ decreased from approximately 2.7 m at 57% to 2.1 m at 76%. The dashed graphs represent the numerically predicted displacements
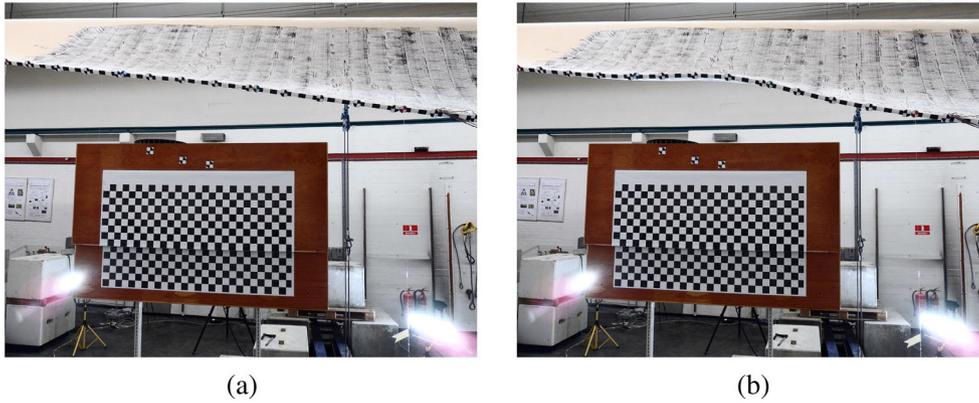
Figure 11. (a) Trailing-edge deformation at 57% load level with marker points and calibration grid (later) and (b) trailing-edge deformation at 76% load level with a distinct wave peak.
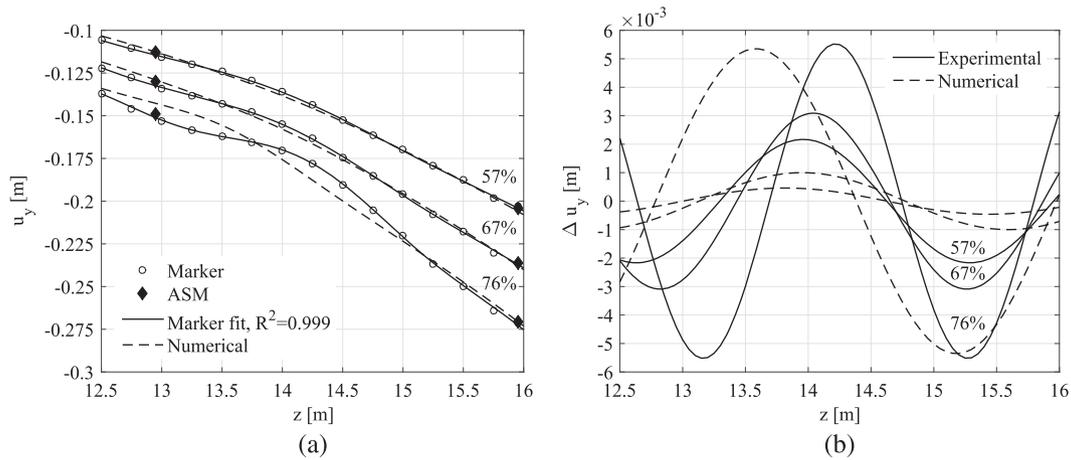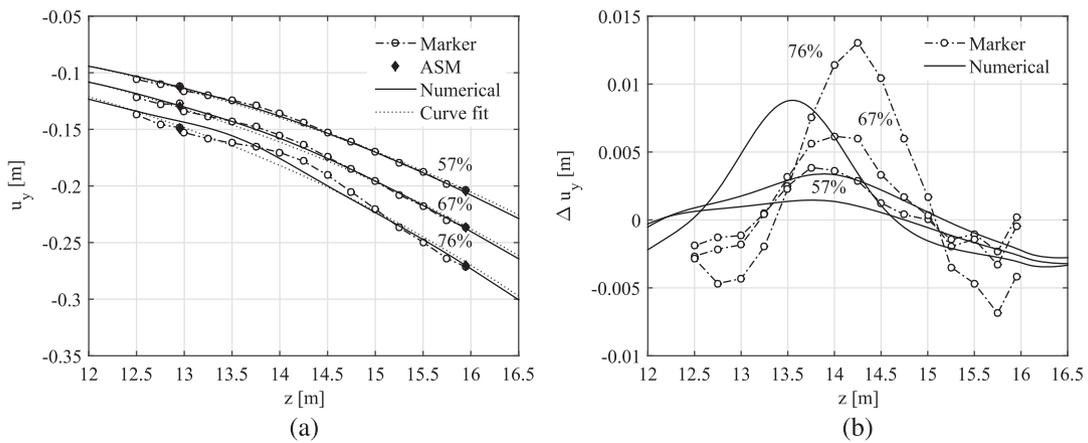

Figure 12. (a) Comparison of measured global vertical trailing-edge displacements u_Y of marker points and ASMs with numerically obtained displacements for three different load levels and (b) comparisons of local deformation wave given by $\Delta u_Y(z) = a_3 \sin(fz)$ extracted from measurements and numerical analysis.

Figure 13. (a) Comparison of measured global vertical trailing-edge displacements u_Y of marker points and ASMs with numerically obtained displacements for three different load levels and (b) comparison of local deformation $\Delta u_Y(z)$ as offset from a curve fit through the global displacement extracted from the numerical analysis.

post-processed using the same procedure. Figure 12(a) shows that the numerical model appropriately predicts the measured response for 57%. The deviation increases with increasing load as the model predicts the wave peak at a different location. Figure 12(b) shows a likely prediction of the amplitude at 76%.

The results of the local wave as found by the hybrid wave extraction approach (Section 2.7) are shown in Figure 13(a) and (b). The base deformations given by equation (7) are represented by dotted graphs. The solid graphs represent the numerically predicted deformations and the circular markers represent measurement results. Figure 13(b) compares the measured and numerically predicted deflections subtracted from the numerically determined base deformations. It shows that the numerically predicted early wave amplitudes correspond to those obtained from measurements. The numerical model predicted the location of the positive wave peak reasonably well at an offset of 0.7 m (Figure 13(b)). Whilst the model underestimated the amplitude for higher load levels (76%), it deviated insignificantly for lower ones. The reason for the deviation for higher loads can be explained by observation during the experiment. The trailing-edge wave caused a kink in the pressure side panel inducing high transverse deformation gradients, which caused local panel failure prior to trailing-edge debonding. The model did not account for the local stiffness degradation caused by panel failure. Hence, wave amplitudes were underpredicted for higher load steps because of overprediction of transverse stiffness.

The comparison of the experimental trailing-edge response with the numerical prediction in Figure 14(a) and (b) shows that the latter underpredicts the amplitude because stiffness degradation was not taken into account.

Figure 15(a) and (b) compares the measured and numerically obtained ϵ_{11} and ϵ_{22} strain distributions at a load level of 57%. FBG measurements for load steps higher than 57% are not presented because ϵ_{22} measurements exceeded the measurement range of the sensors.

The ϵ_{11} measurements show considerable fluctuations between 10.0 and 13.5 m, whereas the remaining data are more consistent. It was found that the sensors in the noisy area were placed on the sandwich core region of the trailing-edge panel, while the remainder was placed on the pure laminate (Figure 16). The different placements were inevitably caused by the variation of the sandwich core width along the blade, which interfered with the constant offset of the sensors from the trailing edge. It is conjectured that the fluctuations are related to local strain concentrations induced by gaps in the material, which are more likely to occur in the sandwich core than in the pure laminate. Figure 15(a) shows that the model, which does not take micro defects into account, predicts the average of the measured strains that corroborates the conjecture. Furthermore, it can be seen that ϵ_{22} levels at the critical wave are higher than the ϵ_{11} strains, which are consistent with the

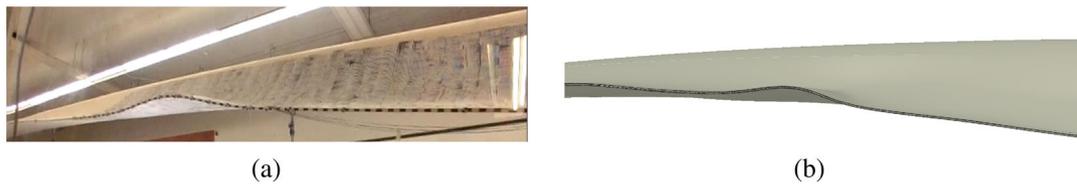(a)   (b)

Figure 14. (a) Trailing-edge deformation during the blade test at the 100% load step and (b) numerical result showing the trailing-edge deformation at the same load step.
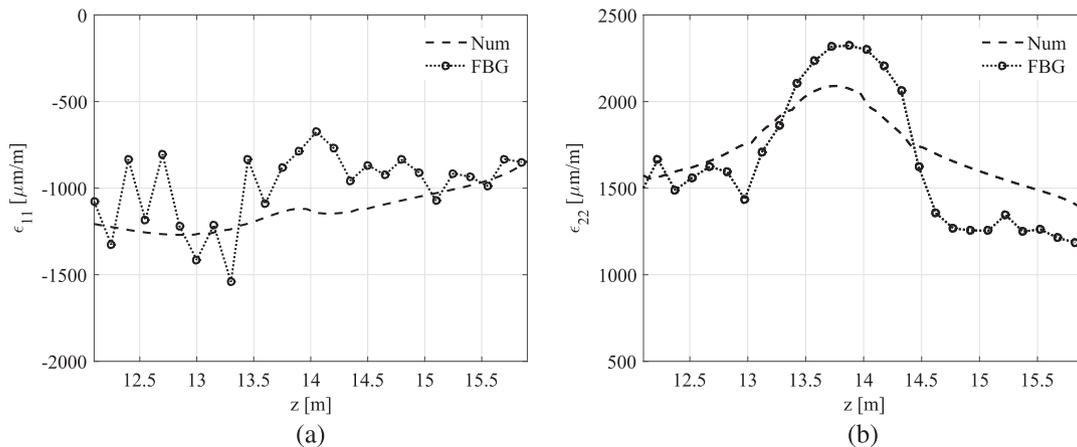

Figure 15. Measured (at 0.15 m spacing) and numerically predicted longitudinal strain ϵ_{11} (a) and transverse strain ϵ_{22} (b) along trailing edge at 57% load steps. FBG, Fibre Bragg Grating.
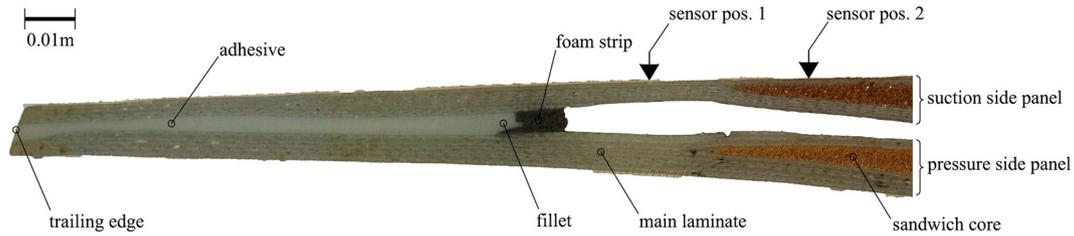
Figure 16. Trailing-edge slice extracted from the tested wind turbine blade showing adhesive joint between pressure side and suction side shells with sensor location on the pure laminate (sensor pos.1) and above the sandwich core (sensor pos.2).
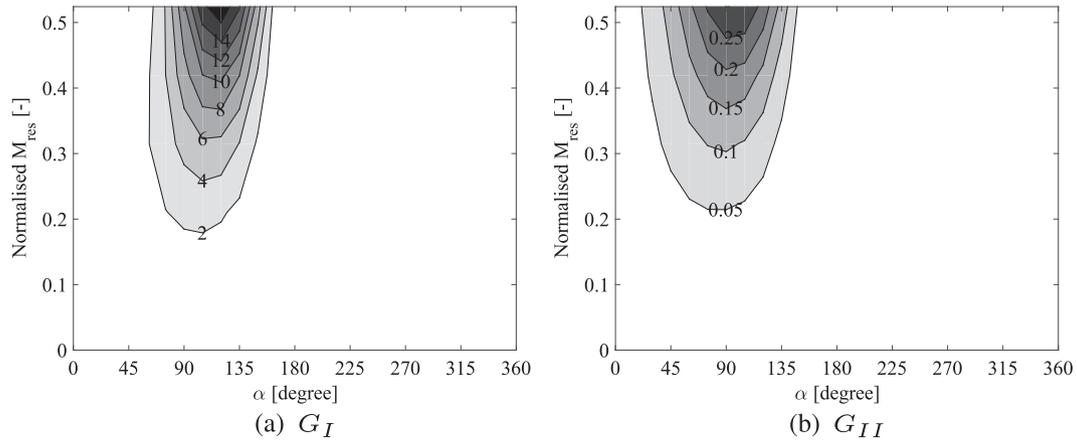

(a) G_I

(b) G_{II}

Figure 17. (a) and (b) Strain energy release rate contour plots as function of the constant bending moment under different angular directions with its angle α and its normalized bending moment magnitude.

aforementioned excessive transverse deformations. The comparison between the numerical prediction and the experimental measurements results in reasonable good agreement.

3.3. Fracture analysis results

The model was subsequently used to investigate the structural behaviour of the blade subject to the *CBM* and *MDL* load envelopes for a complete 360° revolution in angular increments of $\Delta\alpha = 15°$. Figures 17(a) through 18(b) show SERRs extracted at the peak of the critical buckling wave as it appeared in the model at 13.0 m upon ultimate loading. The bending moment magnitude represents 57% of the ultimate bending moment in the 13.0 m cross section and represents the measurable onset of wave formation. The constant bending moment distribution at 57% was chosen to investigate the effects of in-plane cross-section warping without the influence of the wave, in order to make the results comparable with previous studies. Figure 17(a) and (b) shows two distinct G_I and G_{II} ridges whose maxima occur between $\alpha = 90°$ and $\alpha = 120°$. Figure 18(a) shows three small G_{III} ridges occurring at $\alpha = 45°$, 150° to 165° and 255°. The out-of-plane shear (mode-III) seemed to occur regularly every 90°. Figure 18(b) shows a critical angle of $\alpha = 120°$ for the constant bending moment with a low utilisation level of G_{equ} and another small peak at $\alpha = 255°$. The first peak occurring in quadrant QII is mode-I dominated as shown in Figure 17(a), whereas the second peak is governed by mode-III SERR as shown in Figure 18(a).

Figure 19(a) shows two peaks, the first occurred at $\alpha = 135°$ and reaches approximately 20% of the critical energy level. The second peak occurred at $\alpha = 240°$. The plots show that the second peak exceeds G_{equ}. In Figure 19(b), the mode-mixities ϕ and ψ were plotted for the MDL envelope evaluated at 13.0 m. For $\alpha = 135°$ the in plane mode mixity is mode-I dominated, whereas between $\alpha = 225°$ to $\alpha = 245°$ mode-III prevails.

Figure 20(a) through (b) shows SERRs obtained for MDL along the crack front between 12.25 and 13.75 m for $\alpha = 135°$. This direction yields the highest mode-I SERR levels for both CBM and MDL. Under this load direction, G_I is significantly higher than G_{II} and G_{III}.

Figure 21(a) through (b) shows SERRs obtained for MDL along the crack front between 12.25 and 14.5 m for $\alpha = 240°$. This direction provokes the highest wave amplitudes in the trailing edge, thus maximizing the impact on the SERRs.
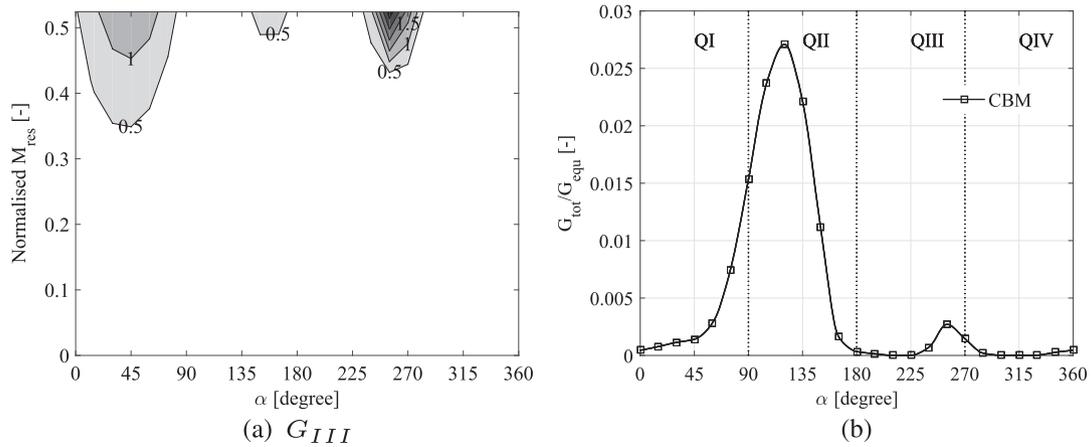
(a) G_{III}

(b)

Figure 18. (a) Strain energy release rate contour plot as function of the constant bending moment (CBM) under different angular directions with its angle α and its normalized bending moment magnitude and (b) G_{tot}/G_{equ} as a function of the bending moment vector angle α and its magnitude subdivided into four quadrants indicated by dotted lines for a CBM.
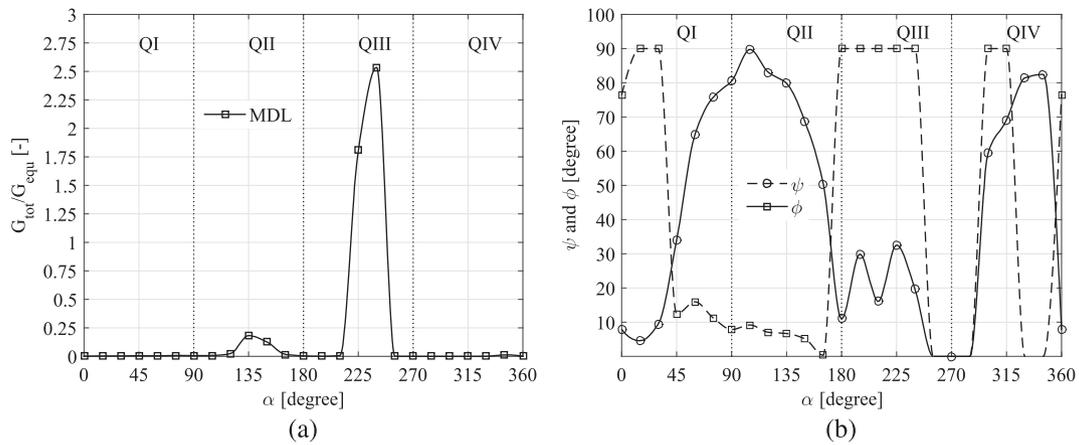

(a)

(b)

Figure 19. (a) G_{tot}/G_{equ} plot of maximum design load (MDL) and (b) mode-mixities as function of the bending moment angle α for MDL.
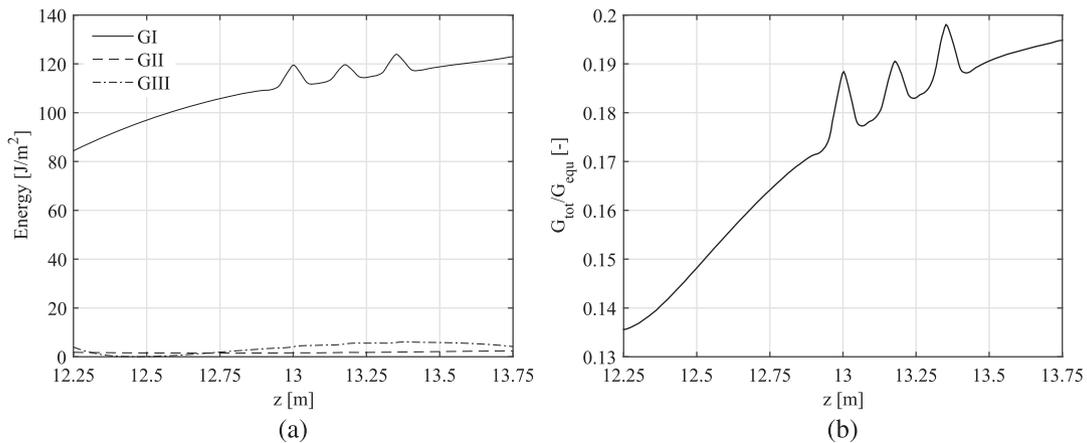

(a)

(b)

Figure 20. (a) Modal strain energy release rate distributions for maximum design load for $\alpha = 135°$ and (b) the corresponding G_{tot}/G_{equ} distribution.
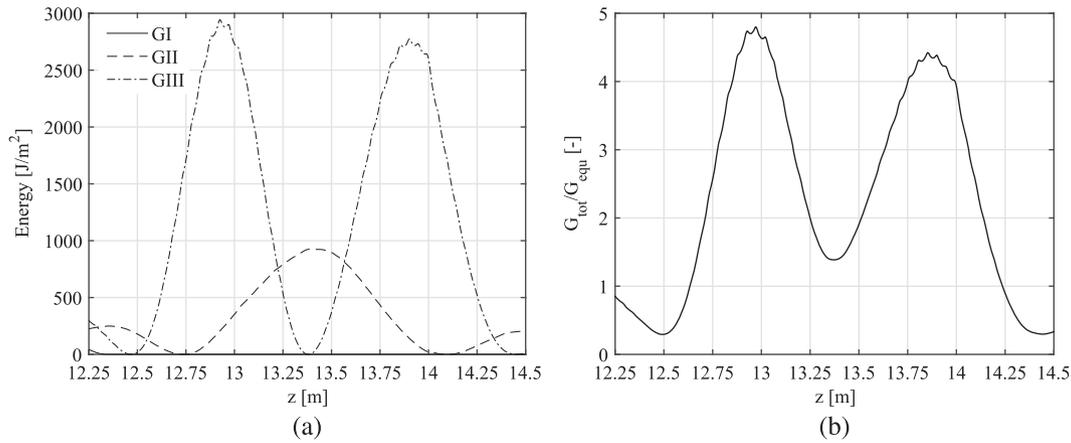
Figure 21. (a) Strain energy release rate distributions for maximum design load for α = 240° and (b) the corresponding G_{tot}/G_{equ} distribution.
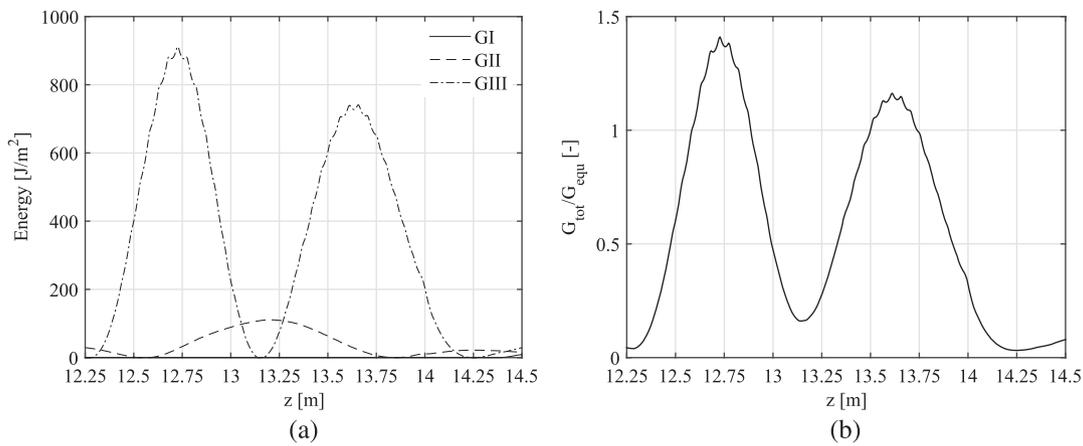

Figure 22. Strain energy release rate distributions for the experimental loading condition with α = 210° and the corresponding G_{tot}/G_{equ} plot.

Whereas the SERR levels of CBM were negligibly small, they increased significantly for MDL. Figure 21(a) shows that G_I was negligible but that G_{II} and G_{III} values increased significantly with mode-III governing the mode mixity. Figure 21(b) shows that the critical peaks occurred at around 12.75 and 13.8 m. The critical G-III peaks flanked the trailing-edge wave deformation at 13.29 m. At 13.29 m, the G_I and G_{III} were suppressed and G_{II} increased instead.

Similar behaviour was observed for the experimental load direction of 210° and under the previously described load conditions as shown in Figure 22(a) and (b). Here, the maximum trailing-edge deformation at UL was located at 13.15 m.

Figure 23(a) and (b) shows in-plane warping deformations of the trailing-edge panels under MDL for α = 135° and α = 240°, with a cutting plane in the most critical locations at 13 and 13.30 m, respectively. Figure 23(a) shows a mode-I opening under α = 135°, whereas the wave under α = 240° suppressed mode-I by the panel being closed.

4. DISCUSSION

Measurement data of displacements and strains show that a longitudinal wave occurred in the trailing edge at an unexpectedly early loading stage. The numerical model predicted the location of the positive wave peak reasonably well at an offset of 0.7 m (Figure 13(b)). The reason for the deviation for higher loads can be explained by damage induced by stiffness degradation of the trailing-edge panels near the critical wave. Stiffness degradation associated with progressive failure modelling was omitted in the present analysis. More information regarding the influence of panel damage on local wave formation appear in.[28]
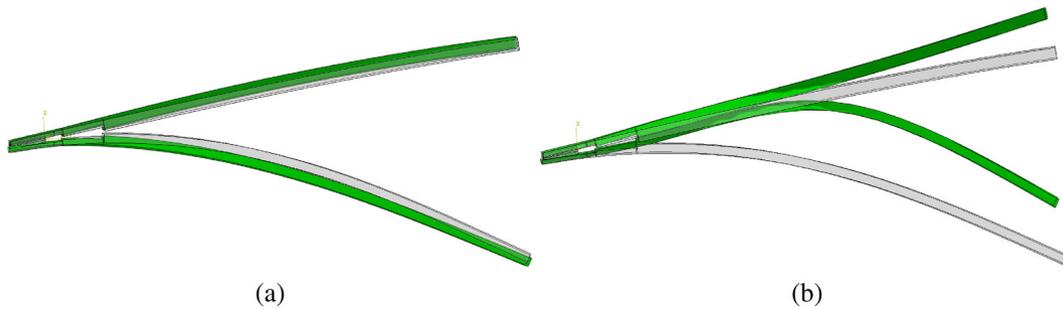
Figure 23. Cross section showing the local in-plane warping deformation of the trailing edge for maximum design load. (a) The trailing-edge deformation (with scale factor 2) for the blade under a bending moment angle of 135° and a cutting plane at 13 m and (b) the trailing-edge deformation for the blade under a bending moment angle of 240° and cutting plane at 13.30 m.

The observed trailing-edge wave formation can hardly be characterized as *bifurcation buckling* as defined in.[29] The wave did not pop up at a critical load as would be expected in a classic bifurcation buckling situation as discussed by Kühlmeier.[30] Instead, the wave formed gradually from an early loading stage on and prevented the identification of post-buckling behaviour. Nor did the observed phenomenon comply with the definition of *limitpoint buckling* stipulated in[29] because the load-deformation relationship did not reach a distinguishable maximum when deformations were increased in an uncontrolled manner. Difficulties of distinguishing buckling phenomena in wind turbines were also described by Cox and Echtermeyer[31] and in greater detail by Lindgaard and Lund.[32]

The G_I and G_{II} ridges shown in Figure 17(a) and (b) can be explained by the Brazier effect as discussed in.[8] It shows that the SERRs in this loading direction are mode-I dominated when the lengthwise bending stresses in the trailing edge are positive (tension). Fracture analysis indicates a critical bending moment range between $\alpha = 90°$ and $\alpha = 135°$ as far as the Brazier effect is concerned. Usually, a second G_I ridge was expected between 270° and 300° but was suppressed by the wave when the bending stresses in the trailing edge were negative (compression).

The G_{tot} levels for cases dominated by mode-I remained well below the G_{equ} values for static crack growth. However, it can be seen from Figure 17(a) for lower load levels (CBM) and in Figure 20(a) for MDL that G_I reaches levels between 80 J m^{-2} and 120 J m^{-2}. These are well within experimentally obtained fatigue thresholds of adhesively bonded double cantilever beam specimens reported by Ishii [33, Figure2] and Azari.[34] Note that the fatigue thresholds were obtained under controlled conditions. The fatigue threshold in wind turbine blades should perhaps be lowered because of flaws induced by manufacturing, and residual stresses caused by curing.

Figure 21(a) to (b) shows that geometrical non-linear wave formation under MDL caused a rapid and progressive increase of the SERRs. In the present case, G_I was suppressed between 12 and 14 m. Instead, G_{III} dominated the experimentally tested load case. Figures 21(b) and 22(b) show that critical G_{tot}/G_{equ} peaks occurred beside the peak of the wave, which in both cases exceeded G_{equ}. This shows that a geometrical non-linear wave in the trailing edge can lead to crack growth under extreme loading conditions. G_{tot}/G_{equ} peaks occurred for both CBM and MDL at qualitatively similar angular directions, which indicates that these directions should undergo further investigations.

Note that torsional aeroelastic moments were not studied in this analysis, which means that G_{III} SERRs are probably underestimated in some cases. Some torsion was induced into the blade by bend–twist coupling and by load eccentricities caused by bend–bend coupling. However, torsional aeroelastic loads should be studied in future investigations.

5. CONCLUSION

The findings can be summarized as follows:

(i) It was shown, both experimentally and numerically, that a geometric non-linear longitudinal trailing-edge wave can occur in blades, which are designed to prevent local buckling. Such a wave can have serious consequences for the integrity of the adhesive trailing-edge joint.

(ii) Surface strain measurements on laminates with FBGs are influenced by local effects (e.g. material imperfections) leading to strain concentrations, and by the alignment between the fibre reinforcement and the FBG sensor.

(iii) Two critical bending moment vector directions exist in the investigated case. The first occurred at $\alpha = 135°$ and is consistent with the Brazier effect reported in.[8] The second occurred at approximately $\alpha = 240°$ and is associated with geometrically non-linear wave formation.

(iv) The numerically obtained G_I levels exceeded experimentally obtained fatigue thresholds of adhesive joints.

(v) The trailing-edge wave suppressed G_I and amplified G_{II} and G_{III}. Such induced SERR levels can lead to adhesive joint failure under maximum design loading conditions.

(vi) Pure flap-wise and pure edge-wise loading directions in blade certification tests might not be sufficient when adhesive joint failure is concerned, tests under combined loading directions should be considered.

(vii) Trailing-edge subcomponent tests should not only examine mode-I fracture, but also mixed mode conditions.

ACKNOWLEDGEMENTS

REFERENCES

1. Ataya S, Ahmed MMZ. Damages of wind turbine blade trailing edge: forms, location, and root causes. *Journal of Engineering Failure Analysis* 2013; **35**: 480–488.

2. Sheng S. *Report on Wind Turbine Subsystem Reliability—A Survey of Various Databases, Technical Report*, NREL/PR-5000-59111, 2013.

3. Wittrup S. *Dong og Siemens giver Horns Rev 2 storstilet vinge-makeover*, 2015. [Online]. Available: http://ing.dk/artikel/dong-og-siemens-giver-horns-rev-2-storstilet-vinge-makeover-173761 (Accessed 18 May 2015).

4. Eder MA, Bitsche RD, Nielsen M, Branner K. A practical approach to fracture analysis at the trailing edge of wind turbine rotor blades. *Wind Energy* 2015; **16**: 1007–1022.

5. Damkilde L, Lund B. A simplified analysis of the Brazier effect in composite beams. In *Proceedings of the Twelfth International Conference on Civil, Structural and Environmental Engineering Computing*, Topping BHV, Costa Neves LF, Barros RC (eds). Civil-Comp Press, 2009. (Civil-Comp Proceedings; No. 91).

6. Cecchini LS, Weaver PM. Brazier effect in multibay airfoil sections. *AIAA Journal* 2005; **43**: 2252–2258.

7. Shmueli J, Eder MA, Tesauro A. A versatile stereo photogrammetry based technique for measuring fracture mode displacements in structures. *Precision Engineering* 2015; **39**: 38–46.

8. Eder MA, Bitsche RD. A qualitative analytical investigation of geometrically nonlinear effects in wind turbine blade cross sections. *Thin-Walled Structures* 2015; **93**: 1–9.

9. Eder MA, Bitsche RD, Belloni F. Effects of geometric non-linearity on energy release rates in a realistic wind turbine blade cross-section. *Composite Structures* 2015; **132**: 1075–1084.

10. Eder MA, Bitsche RD. Fracture analysis of adhesive joints in wind turbine blades. *Wind Energy* 2015; **18**: 1007–1022.

11. Holistic Structural Integrity Process. [Online]. Available http://www.holsip.com. (Accessed 24 September 2015)

12. Hill K, Meltz G. Fiber Bragg grating technology fundamentals and overview. *Journal of Lightwave Technology* 1997; **15**: 1263–1276.

13. Kersey AD. A review of recent developments in fiber optic sensor technology. *Optical Fiber Technology* 1996; **2**: 291–317.

14. Morey W, Meltz G, Glenn H. Fiber optic Bragg grating sensors. *Proc. SPIE 1169, Fiber Optic and Laser Sensors VII*, 1990. DOI: 10.1117/12.963022.

15. Kashyap R. *Fiber Bragg Gratings*. Academic Press: Montréal, Canada, 1999.

16. Schroeder K, Ecke W, Apitz J, Lembke E, Lenschow G. A fibre Bragg grating sensor system monitors operational load in a wind turbine rotor blade. *Measurement Science and Technology* 2006; **17**: 1167–1172.

17. Fattahi SJ, Zabihollah A, Zareie S. Vibration monitoring of wind turbine blade using fiber Bragg grating. *Wind Engineering* 2010; **34**: 721–731.

18. Atkinson KB. *Close Range Photogrammetry and Machine Vision*. Whittles Publishing: Scotland, UK, 1996.

19. Larsen TJ, Hansen AM. Influence of blade pitch loads by large blade deflections and pitch actuator dynamics using the new aeroelastic code HAWC2. *Proceedings of the European Wind Energy Conference*, Athens, Greece, 2006; 1–5.

20. HAWC2—Horizontal Axis Wind Turbine Simulation Code 2nd Generation—Official Website. [Online]. Available http://www.hawc2.dk. (Accessed 1 July 2015)

21. Troldborg N, Bak C, Madsen HA, Skrzypinski W. The DAN-AERO MW Experiments: Final Report. Tech. Rep. Risø-R-1726(EN) *Technical Report*, Risø-DTU, Roskilde, Denmark, 2010.

22. HAWCStab2—Aero-servo-elastic Stability Tool for Wind Turbines. [Online]. Available http://www.hawcstab2.vindenergi.dtu.dk (Accessed 24 April 2015).

23. IEC 61400-1: Wind Turbines—Part 1: Design Requirements, 2005.

24. Dassault Systèmes. *Dassault System. Abaqus Analysis Users Manual, vol. 6.13*, 2014.

25. Krueger P. Virtual crack closure technique: History, approach, and applications. *Appl. Mech. Rev* 2004; **57**: 109–143. DOI: 10.1115/1.1595677.

26. Kenane M, Benzeggagh ML. Mixed-mode delamination fracture toughness of unidirectional glass/epoxy composites under fatigue loading. *Composites Science and Technology* 1997; **57**: 597–605.

27. The MathWorks, Inc., Natick, Massachusetts, United States. *MATLAB and Statistics Toolbox Release 2015a*, 2014.

28. Haselbach PU, Branner K. Effect of trailing edge damage on full-scale wind turbine blade failure. *20th International Conference on Composite Materials, Copenhagen*, Copenhagen, Denmark, 2015; 1–12.

29. DNV-DS-J102: Design and Manufacture of Wind Turbine Blades, Offshore and Onshore Wind Turbines, 2010.

30. Kühlmeier L. Buckling of wind turbine rotor blades, *PhD Thesis*, Aalborg University, 2007.

31. Cox K, Echtermeyer A. Effects of composite fiber orientation on wind turbine blade buckling resistance. *Wind Energy* 2014; **17**: 1925–1943.

32. Lindgaard E, Lund E. A unified approach to nonlinear buckling optimization of composite structures. *Computers and Structures* 2011; **89**: 357–370.

33. Ishi K, Imanaka M, Nakayama H. Fatigue crack propagation behavior of adhesively bonded CFRP/CFRP and CFRP/Aluminium joints. *16th International Conference on Composite Materials*, Kyoto, Japan, 2007; 1–8.

34. Azari S, Papini M, Schroeder J, Spelt J. Fatigue threshold behaviour of adhesive joints. *International Journal of Adhesion and Adhesives* 2010; **30**: 145–159.